Broadband coherent Fourier scatterometry: A two-pulse approach

van der Sijs, T.A.; Rafighdoost, J.; Siaudynite, L.; Urbach, H.P.; Pereira, S.F.; El Gawhary, O.

DOI
10.1063/5.0226043

Publication date
2025

Document Version
Final published version

Published in
Review of Scientific Instruments

RESEARCH ARTICLE | JANUARY 22 2025

Broadband coherent Fourier scatterometry: A two-pulse approach

T. A. van der Sijs ; J. Rafighdoost ; L. Siaudinyte ; H. P. Urbach ; S. F. Pereira ; O. El Gawhary

Rev. Sci. Instrum. 96, 013702 (2025)
https://doi.org/10.1063/5.0226043

Review of Scientific Instruments ARTICLE pubs.aip.org/aip/rsi

Broadband coherent Fourier scatterometry: A two-pulse approach

Cite as: Rev. Sci. Instrum. 96, 013702 (2025); doi: 10.1063/5.0226043
Submitted: 28 June 2024 • Accepted: 22 December 2024 •
Published Online: 22 January 2025

T. A. van der Sijs,[1,a)] J. Rafighdoost,[1] L. Siaudinyte,[2] H. P. Urbach,[1] S. F. Pereira,[1] and O. El Gawhary[1]

AFFILIATIONS

[1] Optics Research Group, Imaging Physics Department, Delft University of Technology, Van der Waalsweg 8, 2628 CH Delft, The Netherlands

[2] VSL Dutch Metrology Institute, Thijsseweg 11, 2600 AR Delft, The Netherlands

[a)] **Author to whom correspondence should be addressed:** T.A.vanderSijs@tudelft.nl

ABSTRACT

We demonstrate a broadband implementation of coherent Fourier scatterometry (CFS) using a supercontinuum source. Spectral information can be resolved by splitting the incident field into two pulses with a variable delay and interfering them at the detector after interaction with the sample, bearing similarities with Fourier-transform spectroscopy. By varying the time delay between the pulses, a collection of diffraction patterns is captured in the Fourier plane, thereby obtaining an interferogram for every camera pixel. Spectrally resolved diffraction patterns can then be retrieved with a per-pixel Fourier transform as a function of the delay. We show the physical principle that motivates the two-pulse approach, the experimental realization, and results for a silicon line grating. The presented implementation using a supercontinuum source offers a cost-effective way to acquire multi-wavelength CFS data over a wide wavelength range, with the potential to improve reconstruction robustness and sensitivity in applications such as dimensional metrology.

I. INTRODUCTION

Scatterometry is a non-imaging optical metrology technique that is known for its non-invasiveness, non-destructiveness, and high repeatability.[1–3] Its speed, *in situ* availability, and cost make it especially suitable for integration in industrial production lines. Among its applications, scatterometry techniques are used for grating characterization, and dimensional metrology in particular. This is exemplified by the broad relevance of gratings as they have diverse applications in spectrometers, laser tuning, pulse compression, waveguide coupling, beam shaping, and alignment and calibration in photolithography, among others.[4,5]

One scheme of scatterometry is coherent Fourier scatterometry (CFS). In this technique, a sample is illuminated by a focused spot using a high-NA microscope objective such that the incident field contains multiple angles of incidence within the NA of the microscope objective,[6–9] in contrast to goniometric scatterometry.[10] The objective recaptures the scattered light in a reflection configuration, after which the light propagates to a camera located at the sample's Fourier plane, where the scattered light is detected. What distinguishes CFS from incoherent Fourier scatterometry is the use of a spatially coherent light source, which results in a smaller spot size and allows retrieving the phase difference between overlapping diffraction orders that are coupled into the objective after reflection from the sample. Using interferometric CFS, the phase of the entire far field can be obtained.[11] While originally established for parameter retrieval of gratings, CFS also extends its utility to the detection of particles or defects on surfaces.[12,13]

With the inverse grating problem in mind, additional information channels of the optical field, such as those provided by broadband data, could reduce uncertainties in the reconstructed parameters. Extending CFS to broadband capabilities is thus of great interest, particularly in combination with other information channels, such as polarization. Although CFS can be extended to a multi-wavelength method by switching between distinct monochromatic sources, this would become unpractical and expensive as soon as the number of distinct sources becomes large (~10). There is not yet a way to perform multi-wavelength CFS with a single source over a broad wavelength range. Tunable lasers could offer a solution, but they have a limited wavelength range, are expensive, and suffer from wavelength drift.[14,15] Monochromating a broadband source, on the other hand, has the downside of losing power, as well as suffering from stray light. White-light interference Fourier scatterometry has

been implemented before[16] although spectrally resolved diffraction patterns are not obtained. Another notable realization of a broadband optical method for acquiring spectrally resolved data involves a dual frequency comb[17] although the dual frequency comb requires a large investment.

A well-known technique by which wavelengths can be resolved using a single spatially coherent broadband source is Fourier-transform spectroscopy.[18] Mainly in the infrared regime, this is an established method,[19] where its applications include analysis of chemical substances. Using a Michelson interferometer, the field is split into two copies with variable time delay. These interfere at the detector, and as a function of the delay, an interferogram is obtained. The spectrum can then be retrieved by Fourier transforming the interferogram.

In this paper, we present and employ a novel two-pulse method to extend CFS to a broadband technique using a spatially coherent broadband source. A pulsed, spatially coherent source is first sent into a Michelson interferometer to create two copies of the same pulse, with possibly a time delay with respect to each other. The two pulses are then sent to a CFS system, in which they travel through a high-NA microscope objective, scatter off the sample, are recaptured by the objective, and finally are detected by a camera. Diffraction patterns are collected with a charge-coupled device (CCD) by scanning the time delay. The acquired set of patterns can then be Fourier transformed as a function of time delay to obtain the spectrally resolved Fourier plane. The physical principle that leads to this Fourier-transform property is described in more detail in Sec. II. Our experimental realization with a supercontinuum source is laid out in Sec. III, including the use of a secondary reference source for wavelength calibration. We show acquired data and extracted results for a silicon line grating in Sec. V. This paper is concluded in Sec. VI.

II. PHYSICAL PRINCIPLE

The two-pulse approach allows us to extract spectrally resolved diffraction patterns from broadband measurements. The underlying physical principle, which stems from Fourier-transform spectroscopy, will be discussed in this section. For reference, one way to achieve our goal could be through interferometry by splitting the incident beam and letting the scattered field interfere with the reference beam (which did not interact with the sample) at the detector. The interference term would contain the desired spectral information, but retrieving this spectral information is feasible only under certain stringent assumptions. Instead, we use the Fourier-transform spectroscopy approach of splitting the incident pulse into two pulses with variable delay and sending them through the same path, scattering off the sample. At the detector, the interference of the two pulses is measured for different delay values, thereby constructing an interferogram. We will show that the resulting interference term, as a function of the delay, is directly related to the spectral angular spectrum.

A. Mathematical model

We start with an input field at some reference plane $z = 0$, which is a linearly polarized pulsed field. We thus use a scalar treatment and denote the field at that plane by $E(x, y, z = 0, t)$. Here, z denotes the optical axis, and x and y are transversal coordinates, while t is time. See Fig. 1 for an illustration of the definitions. To represent the optical field, we use the angular spectrum method, sometimes called the plane-wave expansion. In this method, the field is written as a superposition of plane waves, which is a consequence of the Helmholtz equation being linear. A result of the method is that the angular spectrum is related to the optical field by a Fourier transform. For more details on angular spectrum theory, we like to refer the reader to books such as those by Mandel and Wolf or Goodman.[20,21] The angular spectrum of the input field at temporal frequency ν reads

$$A^{(0)}(\xi_x, \xi_y; \nu) = \int_x \int_y \int_t E(x, y, 0, t) \exp\left[-i2\pi(\xi_x x + \xi_y y)\right] \times \exp\left(i2\pi\nu t\right) \mathrm{d}t\, \mathrm{d}x\, \mathrm{d}y, \quad (1)$$

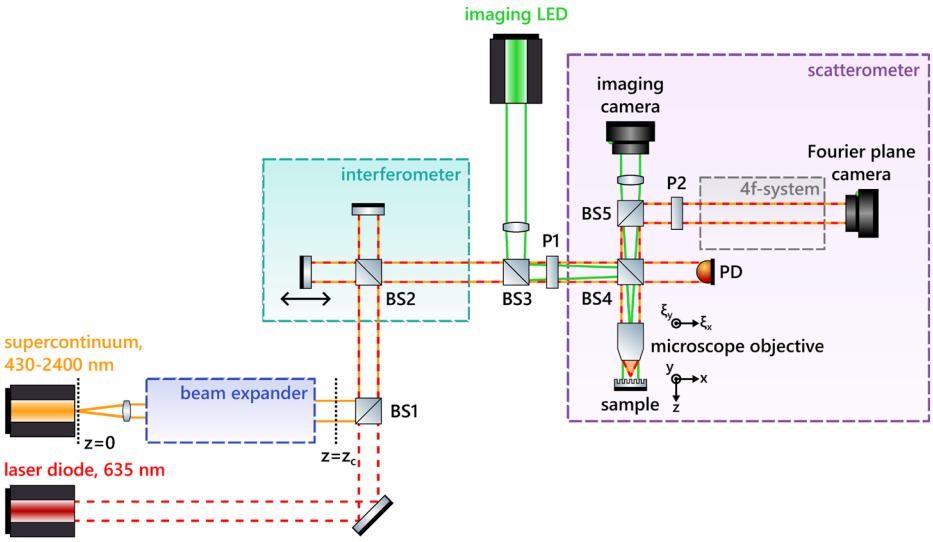

FIG. 1. Schematic illustration of the experimental setup, showing the most important components. The setup's subsystems are depicted by dashed boxes.

where $\xi_x = k_x/2\pi$ and $\xi_y = k_y/2\pi$ are the transverse spatial frequencies. We now collimate $E(x, y, 0, t)$ such that the field after collimation (at $z = z_c$) is a spatial Fourier transform of the input field with respect to the spatial variables x and y. The electric field after collimation thus equals $A^{(0)}$ but evaluated at $\xi_x = s_1 x$, $\xi_y = s_1 y$, with s_1 being some scaling. Summing over all temporal frequencies ν, we have

$$E(x, y, z_c, t) = \int_\nu A^{(0)}(s_1 x, s_1 y; \nu) \exp(-i2\pi\nu t)\mathrm{d}\nu. \tag{2}$$

If we then propagate this collimated field in free space, it collects a global phase factor as we are in the plane-wave regime, but we leave this out for simplicity. Let us say that the collimated field is propagated to a microscope objective, which focuses the field. Depending on the experimental configuration (not specifically considering our two-pulse approach yet), the field then interacts with the sample or a reference mirror, generating a scattered field with an angular spectrum $A^{(s)}(\xi_x, \xi_y; \nu)$. If we account for any propagation over a (possibly varying) distance z_1 in the sample/mirror arm, the angular spectrum reads

$$A^{(s)}(\xi_x, \xi_y; \nu) \exp\left[i2\pi z_1 \sqrt{(\nu/c)^2 - \xi_x^2 - \xi_y^2}\right], \tag{3}$$

where the exponential term is the propagator of reciprocal space. The scattered field is then recaptured by the microscope objective, after which the field propagates to the CCD. At the plane of the CCD, the field (integrated over all temporal frequencies) reads

$$\begin{aligned} E^{(s)}(x, y, z_{\mathrm{CCD}}, t) = &\int_\nu A^{(s)}(s_2 x, s_2 y; \nu) \\ &\times \exp\left[i2\pi z_1 \sqrt{(\nu/c)^2 - (s_2 x)^2 - (s_2 y)^2}\right] \\ &\times \exp(-i2\pi\nu t)\mathrm{d}\nu, \end{aligned} \tag{4}$$

with s_2 again being some scaling parameter for evaluating the angular spectrum in terms of x and y.

B. Two-pulse approach

Now that Eq. (4) shows how a broadband field can be expressed, including propagation of the field and focusing by an objective, we use this to describe the interference of two fields at the detector in a two-pulse approach. The two pulses are generated in a Michelson interferometer, with one arm having a fixed mirror and the other a movable mirror, such that the fields traversing each path travel a different length. As the difference in path length is due to the propagation of a collimated beam in air, the net effect of the path length difference can be equated to a time delay τ between the pulses that vary proportional to the path difference: $\tau = \Delta z/c$, with Δz being the path length difference.

After the two pulses leave the Michelson interferometer, they travel along the same path. As described above, they pass through the microscope objective, interact with the sample, are recaptured by the objective, and finally propagate to the CCD. Along this path, the two pulses therefore do not experience a difference in propagation that would depend on the spatial frequencies, i.e., their angular spectrum is not affected differently. The fields of the two pulses at the detector are thus identical, except that the moving-mirror pulse arrives at the detector with delay τ. Using the notation of Eq. (4), the fields originating from the fixed and moving arm read at the detector ($z = z_{\mathrm{CCD}}$), respectively,

$$\begin{aligned} E^{(s)}(x, y, z_{\mathrm{CCD}}, t) = &\int_\nu A^{(s)}(s_2 x, s_2 y; \nu) \\ &\times \exp\left(i2\pi d \sqrt{(\nu/c)^2 - (s_2 x)^2 - (s_2 y)^2} - i2\pi\nu t\right)\mathrm{d}\nu, \end{aligned} \tag{5}$$

$$\begin{aligned} &E^{(s)}(x, y, z_{\mathrm{CCD}}, t-\tau) \\ &= \int_\nu A^{(s)}(s_2 x, s_2 y; \nu) \\ &\quad\times \exp\left[i2\pi d \sqrt{(\nu/c)^2 - (s_2 x)^2 - (s_2 y)^2} - i2\pi\nu(t-\tau)\right]\mathrm{d}\nu. \end{aligned} \tag{6}$$

where path length d accounts for any propagation distance in the sample arm. At the camera plane, the CCD detects the time-integrated intensity of the sum of the two fields, which reads

$$\begin{aligned} &S(x, y, z_{\mathrm{CCD}}, \tau) \\ &= \int_0^T \left|E^{(s)}(x, y, z_{\mathrm{CCD}}, t) + E^{(s)}(x, y, z_{\mathrm{CCD}}, t-\tau)\right|^2 \mathrm{d}t \\ &= \int_0^T \left|E^{(s)}(x, y, z_{\mathrm{CCD}}, t)\right|^2 \mathrm{d}t + \int_0^T \left|E^{(s)}(x, y, z_{\mathrm{CCD}}, t-\tau)\right|^2 \mathrm{d}t \\ &\quad + 2\,\mathrm{Re}\left\{\int_0^T E^{(s)}(x, y, z_{\mathrm{CCD}}, t)\left[E^{(s)}(x, y, z_{\mathrm{CCD}}, t-\tau)\right]^* \mathrm{d}t\right\}, \end{aligned} \tag{7}$$

with T being the exposure time of the CCD. We rewrite the integral inside the interference term, inserting the Fourier expansion in ν of the two fields,

$$\begin{aligned} &\int_0^T E^{(s)}(x, y, z_{\mathrm{CCD}}, t)\left[E^{(s)}(x, y, z_{\mathrm{CCD}}, t-\tau)\right]^* \mathrm{d}t \\ &= \int_0^T \int_\nu E^{(s)}(x, y, z_{\mathrm{CCD}}, \nu) \exp(-i2\pi\nu t)\mathrm{d}\nu \int_{\nu'} \left[E^{(s)}(x, y, z_{\mathrm{CCD}}, \nu')\right]^* \exp[i2\pi\nu'(t-\tau)]\mathrm{d}\nu'\mathrm{d}t \\ &= \int_\nu \int_{\nu'} E^{(s)}(x, y, z_{\mathrm{CCD}}, \nu)\left[E^{(s)}(x, y, z_{\mathrm{CCD}}, \nu')\right]^* \exp(-i2\pi\nu'\tau) \int_0^T \exp[-i2\pi(\nu-\nu')t]\mathrm{d}t\mathrm{d}\nu'\mathrm{d}\nu \\ &= \int_\nu \int_{\nu'} E^{(s)}(x, y, z_{\mathrm{CCD}}, \nu)\left[E^{(s)}(x, y, z_{\mathrm{CCD}}, \nu')\right]^* \exp(-i2\pi\nu'\tau)\delta(\nu-\nu')\mathrm{d}\nu'\mathrm{d}\nu \\ &= \int_\nu \left|E^{(s)}(x, y, z_{\mathrm{CCD}}, \nu)\right|^2 \exp(-i2\pi\nu\tau)\mathrm{d}\nu = \int_\nu \left|A^{(s)}(s_2 x, s_2 y; \nu)\right|^2 \exp(-i2\pi\nu\tau)\mathrm{d}\nu, \end{aligned} \tag{8}$$

where we approximated the integral over t to a delta function, considering that the integration time of the CCD is very long compared to the oscillations in time of the field. We thus see that the total field in Eq. (7) is the (time-integrated) intensity of both pulses plus the interference term, which is the temporal correlation term,

$$C(x, y, z_{\mathrm{CCD}}, \tau) = 2\ \mathrm{Re}\left\{ \int_{\nu} \left| A^{(s)}(s_2 x, s_2 y; \nu) \right|^2 \exp\left(i 2\pi \nu \tau\right) \mathrm{d}\nu \right\}. \quad (9)$$

This temporal correlation thus contains information about the angular spectrum at frequency ν in the form of a Fourier integral. Essentially, the result is the Wiener–Khinchin theorem.[20]

To put this result into perspective, if we would consider implementing broadband CFS using a white-light interferometric approach, the relation between the interference term and the desired angular spectrum would not be this straightforward. Instead of having a Michelson interferometer before the sample arm, one would interfere the field from the sample arm with the field from a reference arm that contains a moving mirror. In the case of a Linnik-type interferometer, the reference arm contains the same (high-NA) optics as the sample arm to minimalize differences such as aberrations. Now, since the field in the reference arm is strongly focused, the variable delay is a function of spatial frequency in addition to the temporal frequency dependence. In particular, the optical path length difference will be $\Delta z \sqrt{(\nu/c)^2 - \xi_x^2 - \xi_y^2}$ instead of $\nu\tau$ as in Eq. (9). Only by making the strong approximation of assuming plane-wave behavior (i.e., neglecting the dependence on ξ_x and ξ_y) can one retrieve the same Fourier integral as in the two-pulse approach. Without this approximation, it may still be possible to extract the spectrally resolved angular spectrum from the interference term, but this would require a complex mathematical procedure beyond the scope of the methods presented in this work.

C. Extracting the spectral components from the correlation term

To retrieve the desired angular spectrum $|A^{(s)}(s_2 x, s_2 y;\ \nu)|^2$, we first have to isolate the temporal correlation $C(x, y, z_{\mathrm{CCD}}, \tau)$ from the total detected intensity $S(x, y, z_{\mathrm{CCD}}, \tau)$ in Eq. (7) by subtracting the two background intensity terms, acquired by blocking the interferometer arms one at a time. Next, we note that in theory, $C(x, y, z_{\mathrm{CCD}}, \tau)$ is an autocorrelation, so it is an even function of τ. Its Fourier transform thus gives a real function and is exactly equal to $|A^{(s)}(s_2 x, s_2 y;\ \nu)|^2$. Experimentally, misalignments, collimation imperfections, and dispersion effects in the system may affect the interferogram in a way that is not symmetric around the center of the interferogram. This causes the detected interference term $C(x, y, z_{\mathrm{CCD}}, \tau)$ to be asymmetric and its temporal spectrum to be generally complex.[22] We therefore take the absolute value of the complex spectrum that results from Fourier transforming the asymmetric interferogram, thus discarding the wavelength-dependent phase of the power spectral density.[23] Other correction methods are available, as known in the field of Fourier-transform spectroscopy.[24] Finally, the resolution of the spectrum will depend on the range over which τ is scanned, while the step size of τ determines the maximum retrievable frequency.

III. EXPERIMENTAL SETUP

Our experimental implementation of the proposed method at VSL, the Dutch national metrology institute, builds upon a typical monochromatic CFS setup. See Fig. 1 for a schematic depiction of the setup. The main addition is the scanning Michelson interferometer located before the scatterometer, which is used for generating the two identical fields with a variable delay. Furthermore, the setup has two light sources instead of one, a broadband supercontinuum source and a monochromatic laser used for reference, to calibrate the wavelength scale. Light from both sources traverses the interferometer and the scatterometer such that diffraction patterns can be acquired with either source. A third source is present for imaging of the sample, which is useful for sample quality inspection, orientation, and alignment. We will go through the subsystems in limited detail in this section. A full breakdown of the setup is available in the Appendix.

A. Sources

Broadband light is generated using a supercontinuum source (SC-Pro, YSL Photonics) with a spectral output of 430–2400 nm. The source is employed at a repetition rate of 5 MHz for high output power in the visible regime and has power fluctuations that are less than 1%. The beam is collimated and then passes through a beam expander, which is depicted by the blue dashed box in Fig. 1. The broadband light then enters a plate beam splitter (BS1), which is also the point of entry of light from the reference laser (which is collimated at that point). Hence, the collimated beams from the two sources overlap here. We use a 635 nm laser diode (LPS-PM635-FC, Thorlabs) as the reference laser. From here, light from either source travels to the Michelson interferometer. See panel (a) of Fig. 2 for a photo of the setup with the beam path of both sources traced.

The two pulses are generated in a Michelson interferometer with a fixed-mirror arm and a movable-mirror arm. Light is split by a plate beam splitter (BS2) and from there one pulse travels in one arm and another pulse is retarded in the other arm. The movable mirror is mounted on a linear piezo stage and induces the variable time delay between the pulses. The two pulses are combined again at BS2, and the reflected light from the beam splitter (the output of the interferometer) now contains both pulses. Furthermore, a compensating plate is inserted in the fixed-mirror arm.

B. Scatterometer

When the light leaves the Michelson interferometer, it passes a beam splitter (BS3) and propagates to one port of BS3. At the other port of BS3, a third source (a high-power LED) is coupled in, and it is used to image the sample. From this point, the light enters the scatterometer (shown as the purple dashed box in Fig. 1), which is a microscope in epi-illumination configuration. First, the light passes a polarizer (P1) and then enters a beam splitter (BS4), directing part of the beam in transmission to a photodiode (PD). This photodiode is used for locating the point of zero path difference (ZPD) for the two pulses. The rest of the beam is directed toward the high-NA microscope objective (LD Epiplan-Neofluar 0.75 NA, ZEISS), which is infinity corrected and has a long working distance for easier alignment. The setup can be fitted with microscope objectives with various NA.

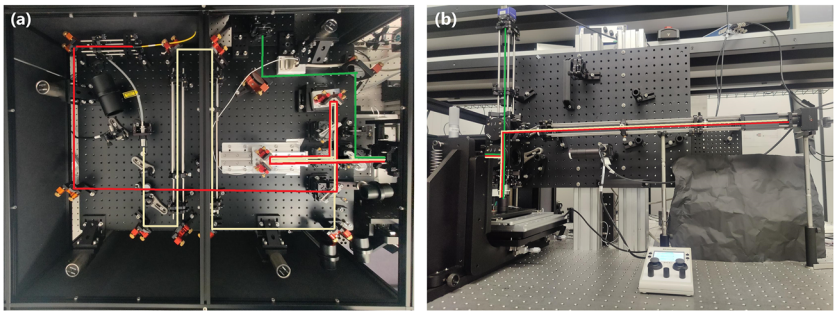

FIG. 2. Photographs of the experimental setup, built at VSL. The white, red, and green lines indicate the light paths of the supercontinuum source, the reference laser, and the LED source, respectively. (a) Top view of the setup, the part containing the sources, and the Michelson interferometer. (b) Side view of the setup, with the vertical part containing the scatterometer.

The sample is mounted on an x, y translation piezo stage, as well as a mechanical tip, tilt, and z stage. The microscope objective focuses the supercontinuum and reference laser light at the top of the sample. When the imaging modality is used, a LED source, which is used for imaging only, is focused on the back focal plane of the microscope objective, providing collimated illumination at the sample. The reflected and scattered field from the sample is recollected by the same objective.

The light transmitted by BS4 propagates to another beam splitter (BS5), where the transmitted beam is diverted for imaging; after another lens, the imaging camera is located in the image plane of the sample. The reflected beam from BS5 passes a second polarizer (P2), then is sent through a 4f system, and finally arrives at the CCD camera that captures the Fourier plane of the sample's top surface. See panel (b) of Fig. 2 for a photo of the scatterometer part of the setup, with the beam path of every source traced.

IV. MEASUREMENT PROCEDURE

Before the diffraction patterns can be acquired, the ZPD position of the interferogram should be known. It can be found rapidly with the photodiode by scanning the moving mirror with the linear stage. Once the ZPD position is found, a scan of the double-sided interferogram is performed around the ZPD. As the interferogram is not symmetric around the ZPD, in practice (see Sec. II), we take the ZPD to be the point of maximum intensity of the interferogram.

Regarding the parameters of the delay scan, the scan range is related to the resolution in the temporal spectrum. The step size of the scan is restricted by the Nyquist sampling theorem as every fringe in the interferogram has to be sampled with enough points. More precisely, the theorem requires that the step size should be smaller than half the smallest wavelength present: $\Delta z \leq \lambda_{\min}/2$.[23] Given that our minimum detected wavelength is 430 nm, we have a maximum of $\Delta z = 215$ nm. The step size of the moving-mirror stage should be no larger than half of this since the light traverses the arm twice.

To complete one full measurement, we need one scan with the supercontinuum source and one with the reference laser. The scans are performed with a step size of 80 nm, which corresponds to a roundtrip change in path length of 160 nm, thus satisfying the Nyquist sampling theorem. The scan with the supercontinuum source is done over a range of 200 μm, taking around 20 min. For the scan with the reference laser, a shorter scan suffices; since it is a monochromatic source, the interferogram will be sinusoidal, so in principle, only a few tens of fringes need to be detected to retrieve the location of its spectral line in the temporal Fourier spectrum. With the reference laser, we scan 20 μm, taking about 3 min. Since the limited measurement range gives a windowed version of the full interferogram, the retrieved spectrum of the reference laser will

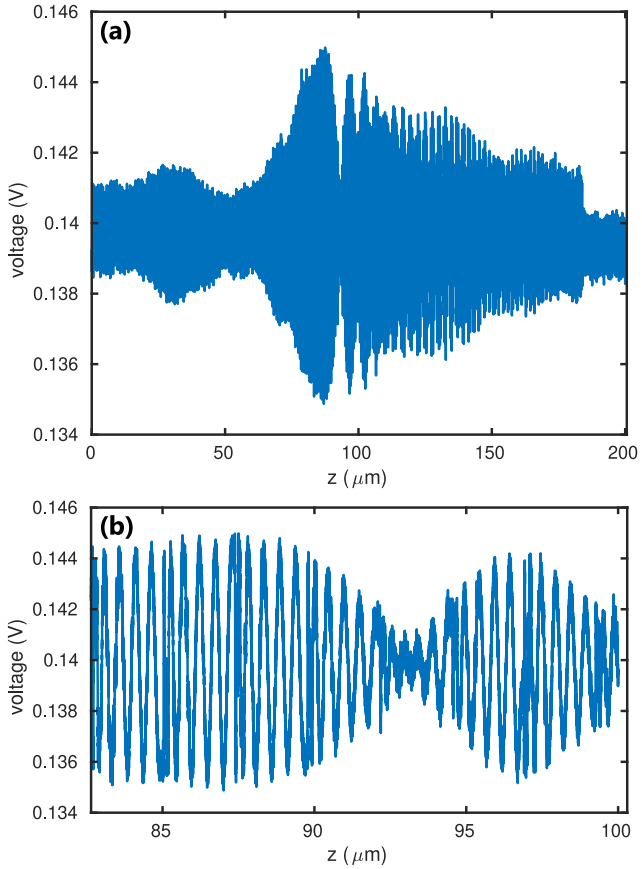

FIG. 3. Interferogram measured by a photodiode, read out with an acquisition card-out at 50 kHz while the moving-mirror stage was moving at 40 μm/s. (a) Interferogram over the full 200 μm range and (b) partial interferogram around the ZPD, showing the fringes of the interferogram.

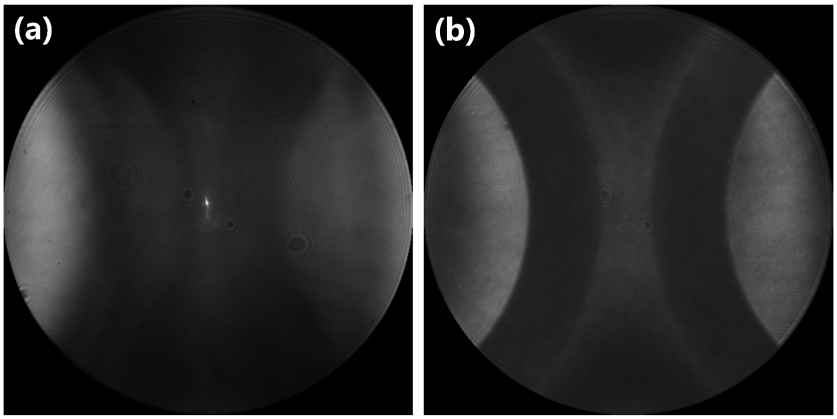

FIG. 4. Examples of far fields collected during the scans with either of the two sources for a 1D grating: (a) broadband source and (b) reference laser. The broadband far field has blurred +1 and −1 diffraction orders because for every wavelength present, the displacement of the orders relative to the center varies.

resemble a $\sin c$ (or actually $\sin c^2$) function, the Fourier transform of the rectangle function.[22]

Finally, to retrieve the angular spectrum according to the derived Fourier transform relation, we must first subtract the background field for each of the two interferometer arms. Hence, for each laser, we also acquire two images by blocking one arm after the other while ensuring that the same CCD exposure time is used as during the respective scans. The two background images are acquired only at the point of zero path difference.

V. RESULTS

In this section, we will show acquired and processed results for a one-dimensional (1D) grating. We will describe the pre-processing of the data, the extracted single-wavelength data, and an analysis of the acquired results. The sample used is a silicon grating with a rectangular profile and a pitch of 589 nm. It has a nominal height of 160 nm and a linewidth of half the pitch. The measurements are done for TM-polarized input light (i.e., the polarization at the pupil of the objective is linear with its direction perpendicular to the grating lines) and TM-polarized output. The polarization is set by polarizers P1 and P2 in Fig. 1.

A. Photodiode data

As explained in Sec. IV, we start by locating the ZPD position using the photodiode, which is read out by an acquisition card (CompactDAQ, National Instruments) at 50 kHz. See the acquired interferogram in Fig. 3 as well as a zoomed-in version of it, which shows the interference fringes. As mentioned in Sec. II, experimental inaccuracies, such as misalignments, cause the interferogram to be not symmetric around the point of ZPD.

B. Fourier-plane data

The broadband scan over a 200 μm range yields 2501 images, while the 20 μm scan with the reference laser yields 251 images. See Fig. 4 for an example of images acquired with the supercontinuum source and with the reference laser. The +1 and −1 diffraction orders are visible, but in the measured far fields for the broadband light, the borders of the diffraction orders are blurred. This is because for every wavelength present in the signal, the position of the +1 and −1 diffraction orders varies, being more displaced from the center for shorter wavelengths.

C. Retrieval of the temporal spectrum

After acquisition of the two scans and the background measurements, the data are pre-processed. Every image is cropped to the size of the pupil, and a fitted circular mask is applied to the pupil to set the pixel values outside the pupil to zero. The two background intensities are subtracted from every image acquired in the scan. The same background images are used for every point in the scanned range. Then, the Fourier transform is taken for every pixel along the axis of time delay τ. As discussed in Sec. II, the Fourier transform of the interferogram will be complex valued. We take the absolute value of this to obtain the spectral density. This procedure is repeated for both the white-light and reference scan.

In order to calibrate the wavelength using the reference scan, we sum the intensity of each image across all pixels within the pupil, resulting in one-dimensional data. Subsequently, we extract the peak of the reference laser and its position in the Fourier domain fixes the values on the wavelength scale. This is done by linearly spacing the Fourier domain, in terms of frequency ν, between 0 and the frequency of the reference laser. Possibly, the location of the peak can be located more accurately by smoothing the Fourier transformed signal by zero-padding of the reference interferogram, yielding a $\sin c^2$ function.

D. Extracted temporal spectrum

The Fourier transformation of the 2501-image white-light dataset yields 2501 spectrally resolved images. Due to the spectral output of the supercontinuum source and the spectral response of the system, only a part of the visible regime has a strong enough spectral response to surpass noise levels. In Fig. 5, we show the extracted spectrum, which is integrated over all camera pixels inside the cropped pupil. It is plotted as a function of wavelength, with the dashed gray line showing the location of the reference laser peak. Only wavelengths below 1000 nm (as above it the response of the silicon CCD reduces dramatically) and above 400 nm are shown. The peak at which total intensity is the highest is 781 nm, according to the wavelength scale deduced from the reference peak.

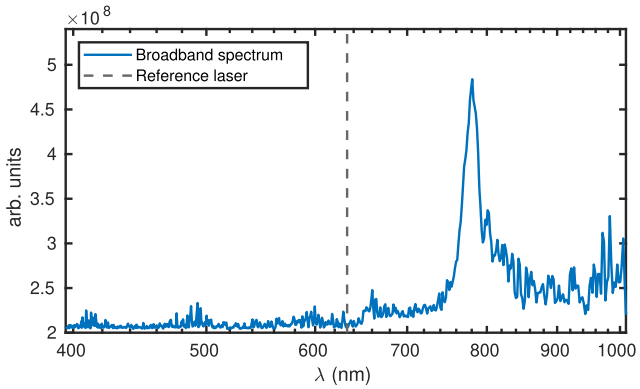

FIG. 5. Extracted spectrum as a function of the wavelength, integrated over the whole pupil. The vertical dashed line indicates the location of the peak of the reference laser (635 nm), used to calibrate the wavelength scale.

Three retrieved images are shown in Fig. 6: at $\lambda = 754$ nm, at $\lambda = 781$ nm (where intensity is the highest), and at $\lambda = 824$ nm. In the first image, the +1 and −1 diffraction orders fall barely inside the pupil, while for shorter wavelengths, they move more and more inside the pupil, whose extent is determined by the microscope objective's NA.

Furthermore, we simulated the scattered field for a silicon grating using rigorous coupled-wave analysis (RCWA) for comparison with the results extracted from the broad wavelength range. Figure 7 shows results for a wavelength of 781 nm, corresponding to the extracted far field in Fig. 6, and for 635 nm, corresponding to the reference laser. Both at input and output, the field is TM polarized. For the simulations, we consider the nominal NA of 0.75 and the aforementioned nominal parameters of the measured silicon grating.

VI. DISCUSSION

We have presented and demonstrated a broadband coherent Fourier scatterometer using a spatially coherent supercontinuum source. Making use of the principle that underlies Fourier-transform spectroscopy, we generate two pulses in a Michelson interferometer with the variable time delay between them. By scanning the moving mirror, we obtain an interferogram at the Fourier-plane CCD from which the spectrally resolved Fourier-plane images are simply retrieved through a Fourier transform as a function of the delay. A scan with a reference laser calibrates the wavelength scale of the retrieved spectrum. For measurements of a silicon 1D grating, retrieved diffraction patterns are spectrally resolved over a 750–825 nm range at 48 distinct wavelength values. A broader range can be obtained by increasing the operation power of the supercontinuum source.

Although currently the scan time is 20 min, the system could be reimplemented to make it effectively "real-time," given a high enough budget. Since the fundamental pulse width is 100 ps, the minimum acquisition time is 200 ps. With a fast-acquisition camera and a fast piezo-stage, the scan time can be considerably reduced since the available laser power is a few watts. Using a fast-acquisition camera with the current piezo-stage could reduce the full scan of 2501 images to <1 s, and a faster piezo-stage could further shorten this time.

Regarding the computational load of the image post-processing, the computational complexity is dominated by the Fourier transform. The complexity of the fast Fourier transform algorithm is $N^2 \times 3M \log_2 M$, with N being the number of pixels along one side of the image and M being the number of images. The computational load could be reduced by first binning the CCD pixels. If the images are used for grating characterization through model-based reconstruction, the current image dimension of 537 × 537 can be binned in a 4 by 4 box without loss of performance. This alone results in a 16× speedup.

This system also enables applications that require lateral sample scanning as the sample stage has a $100 \times 100\ \mu m^2$ lateral scanning range. The delay line as a third scanning dimension increases acquisition time significantly, and improvements in acquisition speed should be made for this method to become attractive for such applications. Other applications include ptychography for phase retrieval as it also uses diffraction patterns for sample reconstruction. The presence of both the broadband and the reference laser allows both single- and multi-wavelength ptychography. The size of the datasets can also pose limitations for lateral sample scans in two dimensions as one delay line scan yields about 5 GB of data. Binning the CCD pixels can reduce the size of the data significantly.

Multi-wavelength CFS data over a broad range has the potential to improve reconstruction robustness when performing model-based parameter retrieval of nanostructures. Given the retrieved wavelength range with our setup, a subset of the resolved diffraction patterns can be taken at desired wavelengths for use in the reconstruction. This flexibility is enabled by our implementation with a

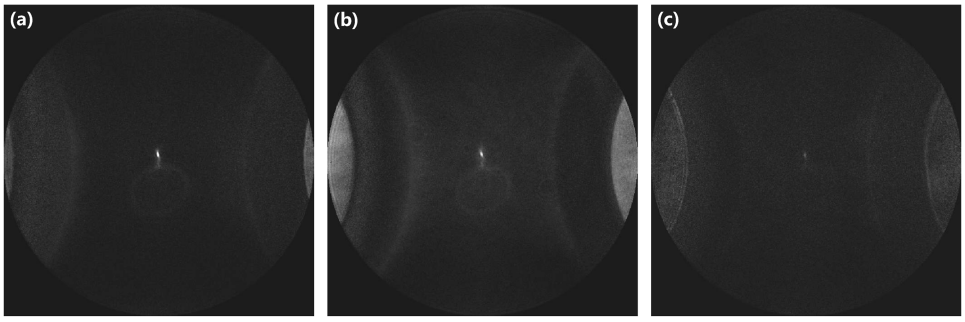

FIG. 6. Extracted Fourier-plane images for a 1D silicon grating at three different wavelengths over a 70 nm range: (a) $\lambda = 824$ nm, (b) $\lambda = 781$ nm, and (c) $\lambda = 754$ nm. The intensity of each image is normalized. The shifting locations of the parts of the ±1st diffraction orders that are captured by the microscope objective are an evident proof of the different wavelengths extracted in each image.

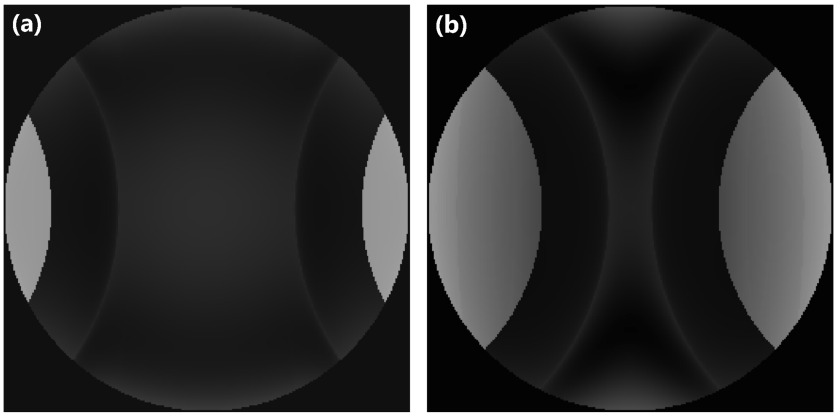

FIG. 7. RCWA simulations for a silicon grating with a pitch of 589 nm and a height of 160 nm. The illumination is TM polarized at input and output. Wavelength used: (a) $\lambda = 781$ nm (center wavelength in Fig. 6) and (b) $\lambda = 635$ nm (wavelength of the reference laser).

supercontinuum source, which moreover makes it a cost-effective method.

ACKNOWLEDGMENTS

This work was partially funded by the Dutch Research Council (NWO) as part of the research program Synoptic Optics (Grant No. P17-24 project 3). Project 20FUN02 POLight, co-financed by the Participating States and from the European Union's Horizon 2020 research and innovation programme. We thank Petro Sonin for providing help in the early phase of the design and the realization of the instrument. We thank Arthur S. van de Nes for writing part of the data acquisition code. We would like to thank Thomas Siefke from the Friedrich Schiller University Jena for fabrication and pre-characterization (by SEM) of the line grating used in this research.

AUTHOR DECLARATIONS

Conflict of Interest

The authors have no conflicts to disclose.

Author Contributions

T. A. van der Sijs: Data curation (lead); Formal analysis (lead); Investigation (equal); Methodology (equal); Software (lead); Visualization (lead); Writing – original draft (lead). **J. Rafighdoost**: Formal analysis (supporting); Investigation (equal); Methodology (equal); Software (supporting); Writing – review & editing (supporting). **L. Siaudinyte**: Investigation (supporting); Resources (lead); Visualization (supporting); Writing – original draft (supporting); Writing – review & editing (supporting). **H. P. Urbach**: Funding acquisition (lead); Writing – review & editing (supporting). **S. F. Pereira**: Funding acquisition (supporting); Methodology (supporting); Resources (supporting). **O. El Gawhary**: Conceptualization (lead); Funding acquisition (supporting); Investigation (equal); Methodology (lead); Project administration (lead); Supervision (equal); Writing – review & editing (supporting).

DATA AVAILABILITY

The data that support the findings of this study are available from the corresponding author upon reasonable request.

APPENDIX: DETAILED DESCRIPTION OF THE EXPERIMENTAL SETUP

The broadband scatterometer developed at VSL consists of five main subsystems: visible 635 nm wavelength illumination and its path, white-light illumination within the range 430–2400 nm and its path, visible 525 nm illumination and its path, Fourier-plane imaging arm, and sample image plane arm. A tip/tilt/z sample stage is also part of the setup.

1. Sources

a. Reference laser

A pigtailed laser diode (LPS-PM635-FC, Thorlabs) generates 635 nm light. The diode is controlled by a driver (CLD1010LP, Thorlabs) temperature-controlled within 0.005 °C. The light enters the setup via a single-mode fiber (1). The light is directed to an achromatic doublet (2 - AC254-100-A-ML, Thorlabs). See Fig. 8. Then, the light is redirected by round UV-Enhanced aluminum mirrors (3, 4 - PF10-03-F01, Thorlabs) to the 50/50 beam splitter (5). A subsequent identical beam splitter (6) transmits and splits the light accordingly toward the Michelson interferometer. See Fig. 2 for an illustration of the beam paths.

b. Supercontinuum source

The white-light source is a 430–2400 nm supercontinuum source (SC-Pro, YSL Photonics). The laser has a fundamental pulse width of 100 fs and a maximum output power of 8 W. It is employed at a repetition rate of 5 MHz for high output power in the visible regime. The white light enters the setup through the fiber (11) and a reflective optical density filter (11a). After an aspheric lens (14), the light goes through a 400-μm pinhole to an achromatic $f = 300$ mm lens (16). The mirrors (17, 18) redirect the light to another lens and a 400 μm pinhole. After another achromatic $f = 300$ mm lens (21) and two mirrors (22, 23), the white light enters the Michelson interferometer and overlaps with the 635 nm wavelength beam.

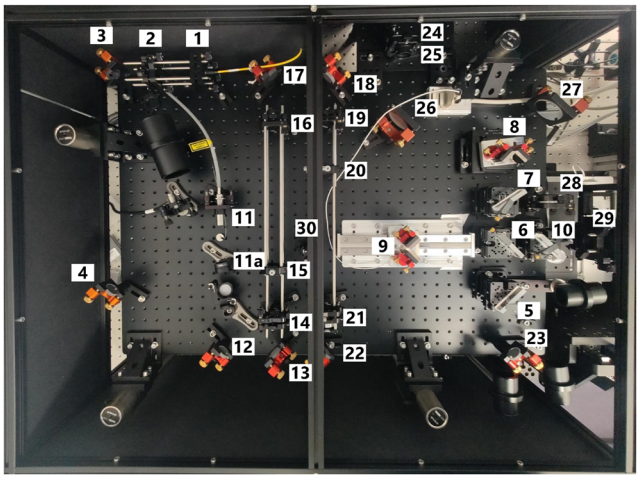

FIG. 8. Illumination part of the setup. The numbers refer to components indicated in the text.

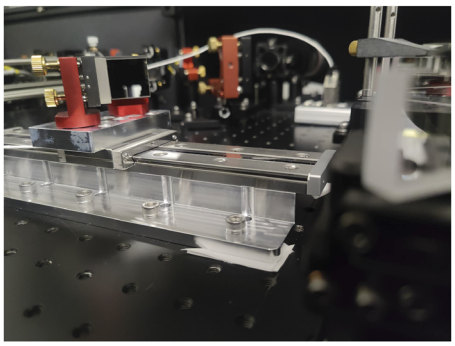

FIG. 9. A close-up photo of the delay line with the paired mirrors and linear piezo-stage.

c. Green LED for imaging

Light from a high-power LED for microscopy illumination at 525 nm (24 - SOLIS-525C, Thorlabs) [shown in green in panel (a) of Fig. 2] enters the setup via an achromatic doublet (25 - AC254-125-A-ML, Thorlabs) and is redirected by 2-in. silver mirrors (26, 27 - PF20-03-P01, Thorlabs) to an achromatic f = 300 mm lens and beam splitter (10) where it overlaps with the two illumination paths mentioned above.

2. Michelson interferometer

Paired mirrors (8, 9) enhance the setup with an internal Michelson interferometer with a fixed and moving arm. See Fig. 9 for a close-up photo of the delay line. The paired mirrors in the moving arm are mounted on a linear piezo stage (CLL42, SmarAct).

After the split beams are recombined in the beam splitter (6), the beam is transmitted via another beam splitter (10) toward the polarizer (29 - WP25M-UB, Thorlabs).

3. Scatterometer

All three beams hit a wedged 2-in. beam splitter (31 - BSW27, Thorlabs), which redirects the light to the microscope objective (32 - LD Epiplan-Neofluar 0.75 NA, ZEISS). See Fig. 10. The microscope objective is infinity corrected and has a working distance of 4 mm. Light is focused on the sample (33), in this case, a one-dimensional (1D) grating, which is mounted on an x, y translation piezo-stage and a mechanical z, tip, tilt stage (34). The linear and the translational piezo-stages are controlled via a control system (MCS2, SmarAct). After interaction with the sample, the light is reflected back to the microscope objective, the beam splitter, and travels further to another 2-inch wedged beam splitter (35 - BSW27, Thorlabs), which splits the beams into two additional arms. Along one arm, the light passes through the polarizer (36 - in the case of single wavelength measurements) and enters an achromatic f = 250 mm lens (37), which focuses on the diffraction pattern generated by the sample in the Fourier plane. Then, the light goes through a pinhole (38) to another achromatic f = 250 mm lens (39) and the diffraction pattern is imaged by a CCD (42 - MD061MU-SY, XIMEA).

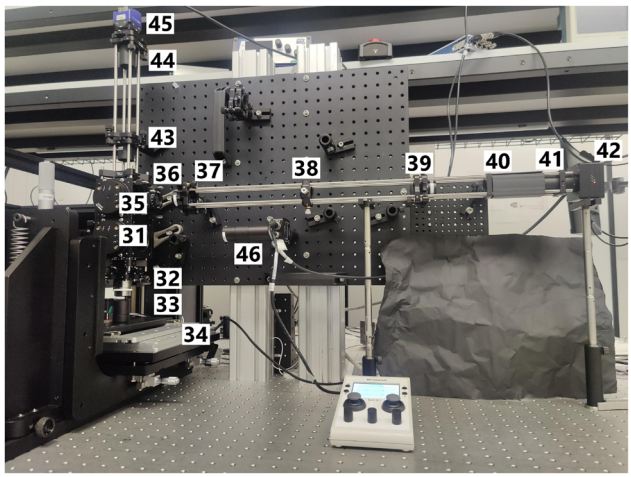

FIG. 10. The scatterometry and microscopy part of the setup. The numbers refer to components indicated in the text.

FIG. 11. Image of the focused spot on a grating on the sample stage, as imaged with the imaging arm of the setup (λ = 525 nm).

The sensor size is 16 mm and the pixel size is 4.54 μm. For an illustration of the beam paths, see panel (b) of Fig. 2. Along the other arm, the beam travels to another achromatic f = 250 mm lens with another camera (45 - mvBlueFOX3, MATRIX VISION) in its focal plane, where the sample is imaged. See Fig. 11 for an example of an imaged grating.

a. Photodiode

A photodiode (46 - PDA36A2, Thorlabs) is placed in the other beam exiting beam splitter (31). The photodiode is read out at 50 kHz using a data acquisition (DAQ) (CompactDAQ, National Instruments).

4. Sample details

The sample is a silicon grating with a pitch of 589 nm. It has a rectangular profile with a duty cycle of 50% and a line height of 160 nm. More detailed information about the fabrication of such nanostructures can be found in Refs. 25 and 26.

REFERENCES

[1] A. C. Diebold, *Handbook of Silicon Semiconductor Metrology*, 1st ed. (Marcel Dekker, Inc., 2001).
[2] C. Raymond, "Overview of scatterometry applications in high volume silicon manufacturing," AIP Conf. Proc. **788**, 394–402 (2005).
[3] M. H. Madsen and P.-E. Hansen, "Scatterometry—Fast and robust measurements of nano-textured surfaces," Surf. Topogr.: Metrol. Prop. **4**, 023003 (2016).
[4] E. G. Loewen and E. Popov, *Diffraction Gratings and Applications* (CRC Press, Boca Raton, 2018).
[5] L. Luo, S. Shan, and X. Li, "A review: Laser interference lithography for diffraction gratings and their applications in encoders and spectrometers," Sensors **24**, 6617 (2024).
[6] O. El Gawhary, N. Kumar, S. F. Pereira, W. M. J. Coene, and H. P. Urbach, "Performance analysis of coherent optical scatterometry," Appl. Phys. B **105**, 775–781 (2011).
[7] S. Roy, O. El Gawhary, N. Kumar, S. F. Pereira, and H. P. Urbach, "Scanning effects in coherent Fourier scatterometry," J. Eur. Opt. Soc.-Rapid Publ. **7**, 12031 (2012).
[8] N. Kumar, O. El Gawhary, S. Roy, S. F. Pereira, and H. P. Urbach, "Phase retrieval between overlapping orders in coherent Fourier scatterometry using scanning," J. Eur. Opt. Soc.-Rapid Publ. **8**, 13048 (2013).
[9] N. Kumar, P. Petrik, G. K. P. Ramanandan, O. El Gawhary, S. Roy, S. F. Pereira, W. M. J. Coene, and H. P. Urbach, "Reconstruction of sub-wavelength features and nano-positioning of gratings using coherent Fourier scatterometry," Opt. Express **22**, 24678–24688 (2014).
[10] J. Endres, N. Kumar, P. Petrik, M. Henn, S. Heidenreich, S. F. Pereira, H. P. Urbach, and B. Bodermann, "Measurement comparison of goniometric scatterometry and coherent Fourier scatterometry," SPIE Proc. **9132**, 913208 (2014).
[11] S. Roy, N. Kumar, S. F. Pereira, and H. P. Urbach, "Interferometric coherent fourier scatterometry: A method for obtaining high sensitivity in the optical inverse-grating problem," J. Opt. **15**, 075707 (2013).
[12] S. Roy, A. C. Assafrão, S. F. Pereira, and H. P. Urbach, "Coherent Fourier scatterometry for detection of nanometer-sized particles on a planar substrate surface," Opt. Express **22**, 13250 (2014).
[13] A. Paul, D. Kolenov, T. Scholte, and S. F. Pereira, "Coherent Fourier scatterometry: A holistic tool for inspection of isolated particles or defects on gratings," Appl. Opt. **62**, 7589–7595 (2023).
[14] B. Mroziewicz, "External cavity wavelength tunable semiconductor lasers—A review," Opto-Electron. Rev. **16**, 347–366 (2008).
[15] F. J. Duarte, *Tunable Lasers Handbook* (Elsevier, 1996).
[16] V. Ferreras Paz, S. Peterhänsel, K. Frenner, and W. Osten, "Solving the inverse grating problem by white light interference Fourier scatterometry," Light: Sci. Appl. **1**, e36 (2012).
[17] E. Vicentini, Z. Wang, K. Van Gasse, T. W. Hänsch, and N. Picqué, "Dual-comb hyperspectral digital holography," Nat. Photonics **15**, 890–894 (2021).
[18] G. R. Fowles, *Introduction to Modern Optics*, 2nd ed. (Dover Publications, New York, 1989).
[19] J. B. Bates, "Fourier transform infrared spectroscopy," Science **191**, 31–37 (1976).
[20] L. Mandel and E. Wolf, *Optical Coherence and Quantum Optics*, 1st ed. (Cambridge University Press, 1995).
[21] J. W. Goodman, *Introduction to Fourier Optics* (Roberts and Company Publishers, 2005).
[22] P. R. Griffiths and J. A. De Haseth, *Fourier Transform Infrared Spectrometry*, 1st ed. (Wiley, 2007).
[23] P. Hariharan, *Optical Interferometry*, 2nd ed. (Academic Press, Amsterdam, Boston, 2003).
[24] M. L. Forman, W. H. Steel, and G. A. Vanasse, "Correction of asymmetric interferograms obtained in fourier spectroscopy," J. Opt. Soc. Am. **56**, 59 (1966).
[25] T. Siefke, L. Siaudinyté, S. A. Jensen, A. T. Rømer, and P.-E. Hansen, "Fine details of structural deviations in reference samples for scatterometry," in *Proceedings of the 19th IMEKO TC10 International Conference on Measurement for Diagnostics, Optimization and Control to Support Sustainability and Resilience*, Delft, The Netherlands, September 21–22, 2023 (IMEKO, 2023), pp. 130–134.
[26] J. Xu, A. D. Refino, A. Delvallée, S. Seibert, C. Schwalb, P. E. Hansen, M. Foldyna, L. Siaudinyte, G. Hamdana, H. S. Wasisto, J. Kottmeier, A. Dietzel, T. Weimann, J. K. Prüssing, H. Bracht, and E. Peiner, "Deep-reactive ion etching of silicon nanowire arrays at cryogenic temperatures," Appl. Phys. Rev. **11**, 021411 (2024).